

7-21-2021

Climate Model Evaluation of Atmospheric Rivers Over the Contiguous United States

Ilan González-Hirshfeld
Portland State University

Follow this and additional works at: https://pdxscholar.library.pdx.edu/open_access_etds



Part of the [Atmospheric Sciences Commons](#), and the [Geography Commons](#)

Let us know how access to this document benefits you.

Recommended Citation

González-Hirshfeld, Ilan, "Climate Model Evaluation of Atmospheric Rivers Over the Contiguous United States" (2021). *Dissertations and Theses*. Paper 5777.

<https://doi.org/10.15760/etd.7648>

This Thesis is brought to you for free and open access. It has been accepted for inclusion in Dissertations and Theses by an authorized administrator of PDXScholar. Please contact us if we can make this document more accessible: pdxscholar@pdx.edu.

Climate Model Evaluation of Atmospheric Rivers over the Contiguous United States

by

Ilan González-Hirshfeld

A thesis submitted in partial fulfillment of the
requirements for the degree of

Master of Science
in
Geography

Thesis Committee:
Paul C. Loikith, Chair
Andrew C. Martin
Martin Lafrenz

Portland State University
2021

© 2021 Ilan González-Hirshfeld

Abstract

Atmospheric rivers (ARs)—long corridors of intense atmospheric water vapor transport—significantly influence the hydrologic cycle and regional hydrometeorological extremes across the contiguous United States (CONUS). Ongoing and future climate change may alter AR characteristics and impacts, making confident climate model projections of future change, especially at regional scales, of critical importance. In order to better constrain uncertainty in such projections of future change, we perform a comprehensive climate model evaluation of AR climatology over the CONUS. Using an established AR detection algorithm, we evaluate the representation of ARs in historical simulations (1984-2013) from a suite of models participating in the sixth phase of the Coupled Model Intercomparison Project (CMIP6). Models are evaluated against the Modern-Era Retrospective Analysis for Research and Applications, Version 2 (MERRA-2) reanalysis. Model performance for individual models and the multi-model mean is presented for AR frequency, intensity, area, and linked extreme precipitation in order to highlight systematic biases. Results are summarized over seven US National Climate Assessment regions. Positive AR frequency biases are present in the Western CONUS for all seasons except summer, with positive biases for the Southeast in summer/spring as well. The Midwest and Eastern CONUS show negative biases in spring and fall, respectively. AR area is systematically overestimated across models, with all regions and seasons showing significant positive biases. AR IVT biases are low for all seasons and regions except the Southwest during winter. ARs in models make up a larger percentage

(positive bias) of extreme precipitation just east of the Sierras in winter/spring than in observations, with negative biases predominating in other seasons/regions. Conversely, ARs are more likely to lead to extreme precipitation in simulations, with the exception of parts of the Midwest and Northern Great Plains in summer. Some positive AR frequency biases may be explained by the large positive AR area biases. Overall, there is reasonable qualitative pattern agreement between MERRA-2 and models in the examined variables, particularly AR frequency and AR IVT.

Acknowledgements

This work was funded, in part, by a NASA Enabling Tools for the NCA grant.

Table of Contents

Abstract.....	i
Acknowledgements.....	iii
List of Tables	v
List of Figures	vi
Chapter 1 Introduction	1
Chapter 2 Data	7
Chapter 3 Methods	9
Chapter 4 Results	12
Chapter 5 Discussion.....	20
Chapter 6 Summary and Conclusion	23
References.....	38

List of Tables

Table 1. Climate model and reference data used in this study. All climate models are from the Coupled Model Intercomparison Project, Phase 6 (CMIP6). Merra-2 and CPC are abbreviated for Modern-Era Retrospective Analysis for Research and Applications, Version 2, and Climate Prediction Center, respectively. Horizontal resolution for CMIP6 models is approximate.....	26
---	----

List of Figures

Figure 1. Map of the study region (the CONUS) and the seven NCA sub-regions examined in the research. Figure from Slinsky et al. (2020).	27
Figure 2. Seasonal AR day frequency maps for the CONUS for (a) MERRA-2, (b) CMIP6, and bias maps for (c) grid points and (d) the NCA regional mean. All values are in units of days/season and each row represents a different meteorological season (winter through fall, from top to bottom). Stippling in column (c) indicates where CMIP6 biases are statistically significant.	28
Figure 3. Mean AR frequency percent biases (y-axis) for each NCA region (x-axis) by model for (a) winter, (b) spring, (c) summer, and (d) fall. The multimodel mean is also shown (black cross). Region abbreviations are in Figure 1.	29
Figure 4. Seasonal median AR area maps for the CONUS for (a) MERRA-2, (b) CMIP6, and bias maps for (c) grid points and (d) the NCA regional mean. All values are in units of km ² and each row represents a different meteorological season (winter through fall, from top to bottom). Stippling in column (c) indicates where CMIP6 biases are statistically significant.	30
Figure 5. Mean AR area percent biases (y-axis) for each NCA region (x-axis) by model for (a) winter, (b) spring, (c) summer, and (d) fall. The multimodel mean is also shown (black cross). Region abbreviations are in Figure 1.	31
Figure 6. Seasonal AR IVT magnitude (shading) and direction (arrows) maps for the CONUS for (a) MERRA-2, (b) CMIP6, and IVT magnitude bias maps for (c) grid points and (d) the NCA regional mean. In column (b), black arrows show CMIP6 IVT direction while gray arrows underneath show MERRA-2 IVT direction for comparison. All shading values are in units of kg m ⁻¹ s ⁻¹ and each row represents a different meteorological season (winter through fall, from top to bottom). Stippling in column (c) indicates where CMIP6 IVT magnitude biases are statistically significant.	32
Figure 7. Mean IVT magnitude percent biases (y-axis) for each NCA region (x-axis) by model for (a) winter, (b) spring, (c) summer, and (d) fall. The multimodel mean is also shown (black cross). Region abbreviations are in Figure 1.	33

Figure 8. Seasonal AR extreme precipitation fraction maps for the CONUS for (a) MERRA-2, (b) CMIP6, and bias maps for (c) grid points and (d) the NCA regional mean. All values are in units of percent and each row represents a different meteorological season (winter through fall, from top to bottom). Stippling in column (c) indicates where CMIP6 biases are statistically significant..... 34

Figure 9. Mean AR extreme precipitation fraction percent biases (y-axis) for each NCA region (x-axis) by model for (a) winter, (b) spring, (c) summer, and (d) fall. The multimodel mean is also shown (black cross). Region abbreviations are in Figure 1. 35

Figure 10. Seasonal AR fraction maps for the CONUS for (a) MERRA-2, (b) CMIP6, and bias maps for (c) grid points and (d) the NCA regional mean. All values are in units of percent and each row represents a different meteorological season (winter through fall, from top to bottom). Stippling in column (c) indicates where CMIP6 biases are statistically significant..... 36

Figure 11. Mean AR fraction percent biases (y-axis) for each NCA region (x-axis) by model for (a) winter, (b) spring, (c) summer, and (d) fall. The multimodel mean is also shown (black cross). Region abbreviations are in Figure 1. 37

Chapter 1 Introduction

Atmospheric rivers (ARs) are filamentary bands of elevated water vapor transport, instrumental for the poleward transport of moisture in the extratropics (Zhu and Newell 1998; Newman et al. 2012), and often associated with the leading edge of a cold front in midlatitude cyclones (Ralph et al. 2017). Research on ARs has received growing attention in the scientific community and their importance to the hydrologic cycle and regional hydrometeorological extremes is well documented in the United States West Coast, where they are associated with both hazards and benefits. In that region, they are linked to heavy rainfall (Ralph and Dettinger 2012), floods and levee breaks (Neiman et al. 2011; Florsheim and Dettinger 2015; Konrad and Dettinger 2017), storm surges caused by associated winds (Khouakhi and Villarini 2016), and severe mass wasting events (Hatchett et al. 2017; Oakley et al. 2017; Young et al. 2017). Conversely, ARs can replenish water supply (Guan et al. 2010; Dettinger et al. 2011), break droughts (Dettinger 2013), and exhibit a variety of ecological impacts (Herbst and Cooper 2010; Florsheim and Dettinger 2015; Albano et al. 2017).¹ In the US, ARs and their effects are not confined to the Eastern Pacific (Slinskey et al. 2020), with several impacts identified elsewhere in the US, including precipitation in the Mississippi Valley (Rabinowitz et al. 2018), precipitation in the southeast US (Miller et al. 2018), and a flooding event in Tennessee (Lackmann et al. 2013).

¹ This list was based on Table 5.1 of Dettinger et al. (2019).

These substantial impacts have prompted multiple studies aiming to assess projected changes in ARs under continued global warming and results suggest potentially substantial changes (Espinoza et al. 2018 and the studies summarized therein; Zhao 2020). Both thermodynamic and dynamic mechanisms are shown to contribute to these projected changes. Increased temperatures due to global warming lead to higher moisture content in the atmosphere through the Clausius-Clapeyron relationship; this in turn can increase IVT—a thermodynamic response identified as a primary cause for higher future AR frequency in some regions (Lavers et al. 2013). Dynamic changes in wind speed and direction as well as shifts in the extratropical jet stream induced by global warming have also been found to produce changes in future ARs (Gao et al. 2015; Gao et al. 2016).

Model evaluations are an important precursor to any complete future climate projection study, as they quantify the biases of historical simulations against observations. This provides a measure of the models' intrinsic ability to faithfully reproduce the phenomenon under study. The present study offers a climate model evaluation specific to ARs in the Contiguous United States (CONUS), informing future projection studies in the same region and constraining their uncertainty. The interpretation of any associated future impacts of projected ARs must take into account the uncertainty of those projections, making the climate model evaluation an integral step in the overall process. The following review of AR climate model evaluations performed to-date places the current study in its broader context.

A handful of studies have investigated model bias in reproducing AR characteristics—most as part of future projection analysis studies. Both overestimation (positive model bias) and underestimation (negative model bias) have been found in simulated AR frequency. Examining landfalling ARs in western North America, Gao et al. (2015) found that models capture seasonal and latitudinal variation in AR frequency well, with an underestimation of springtime AR days in the southwest coast. The sign of biases varied seasonally. Hagos et al. (2015) examined the dynamical core² and grid resolution of two GCMs and generally saw a decrease in AR frequency with higher horizontal spatial resolution. Focusing on the Northeast Pacific coast, Payne and Magnusdottir (2015) evaluated CMIP5 models against two reanalysis products, finding generally positive average frequency bias. Hagos et al. (2016), examining multiple ensemble members of one model, found positive biases in the number of landfalling AR days, which were more pronounced for AR extreme precipitation days. Biases were related in part to an equatorward jet displacement, although the biases in both wind speed and extreme precipitation were found to have little impact on projected future changes. Espinoza et al. (2018) evaluated CMIP5 projections of ARs globally against ERA-Interim reanalysis. They found AR frequency in midlatitude regions to be negatively biased by roughly ten percent in the multimodel mean. Likewise, Guan and Waliser (2017) performed a global model evaluation of models from the Global Energy and Water Cycle Experiment

² The dynamical core is the component of a climate model which solves fluid motion equations that determine atmospheric dynamics and relates them to the model grid (Jun et al. 2018).

(GEWEX) Atmospheric System Study (GASS)–Year of Tropical Convection (YoTC)

Multimodel Experiment. They found that roughly half the models had a notable positive frequency bias while only a few had notable negative biases. Radić et al. (2015), using a unique identification scheme leveraging self-organizing maps to identify IVT patterns associated with ARs, found model AR frequency in British Columbia to display larger errors than other variables (analysis based on five CIMP5 models). Differences in methodology notwithstanding, these at times diverging results can be at least partially explained by the scale and location of differing study areas. They underscore the value in region and scale-specific AR model evaluations. Indeed, Zhao et al. (2020) examined global AR frequency using a new high resolution GCM, finding that while overall agreement with reanalysis was good, significant regional biases of opposite signs existed.

In terms of AR spatial distribution, multiple studies have found generally good agreement between observations and models (e.g. Gao et al. 2015; Payne and Magnusdottir 2015; Guan and Waliser 2017; Espinoza et al. 2018). Other variables tend to show more variability in biases. Radić et al. (2015) found AR precipitation and extreme ARs to be well represented in the models they examined. Broadly speaking, Guan and Waliser (2017) note that coarser models tend to exhibit larger error, but not monotonically. For IVT magnitude, Espinoza et al. (2018) saw a negative bias between 15-25% for global midlatitude AR IVT in the multimodel mean. Guan and Waliser (2017) found IVT to have notably smaller biases than AR frequency, with zonal IVT showing a

slight positive bias. Lavers et al. (2015), while not specifically examining ARs, found IVT to be generally well represented in the multimodel mean of CMIP5 historical runs compared to reanalysis. Norris et al. (2021) evaluated Coupled Model Intercomparison Project Phase 6 (CMIP6) models, finding that most of the examined models underestimated IVT magnitude associated with extreme precipitation in California.

While these studies have proved invaluable in assessing ARs in climate models, a gap in understanding and quantifying how climate models reproduce ARs remains (Waliser et al. 2019), especially on regional scales outside the Northeastern Pacific or Western Europe. In some cases, model biases can be commensurate with projected changes (Gao et al. 2015), highlighting the potential value in bias quantification. The increasing attention paid to other regions and the future climate model projections of ARs necessitates a better understanding of climate model performance specific to ARs for those areas. In particular, Slinsky et al. (2020) established a climatology of ARs in the CONUS, setting the stage for a future climate projection AR study in the same region. In that light, this study evaluates AR climate model performance in the CONUS.

While Guan and Waliser (2017) used their version one algorithm (Guan and Waliser 2015) to perform their global model evaluation, the present study uses their slightly modified version two algorithm (tARget version 2; Guan and Waliser 2018). Our analysis distinguishes itself in two ways that render it relevant and novel: (1) we use the latest generation of CMIP6 climate models, which are not the same as those used in Guan and Waliser (2017). (2) Whereas their study is global, this paper focuses on the CONUS and

examines these variables at much smaller regional levels, namely the seven National Climate Assessment (NCA) regions. Region mean aggregates help illustrate regional variation for all examined variables. This focus addresses the gap in AR climate model evaluations for parts of the US outside the West Coast, allowing potentially meaningful regional model biases obscured on the global scale to become apparent. Moreover, this scale of analysis translates more easily to the scale of local AR impacts. It also informs a concurrent future projection study for the CONUS, which together aim to contribute to the NCA. Figure 1 shows a map of the study area and the relevant NCA regions

Chapter 2 Data

2.1 Reference reanalysis

Modern-Era Retrospective Analysis for Research and Applications, version 2 (MERRA-2; Gelaro et al. 2017) serves as the reference dataset for objective AR identification.

Originally on a 0.5° latitude \times 0.625° longitude grid mesh, MERRA-2 data were rescaled to a $1.5^\circ \times 1.5^\circ$ grid using bilinear interpolation. To facilitate comparison with climate models, MERRA-2 data were interpolated to daily resolution from hourly timesteps.

For the precipitation reference, a gauge-based rather than reanalysis-based dataset was chosen, namely the Climate Prediction Center (CPC) Global Unified Gauge-Based Analysis of Daily Precipitation (Xie et al. 2007; Chen et al. 2008a; Chen et al. 2008b)³.

Since primarily 3-day precipitation totals are used in the analysis, we consider the effects of any temporal offsets between MERRA-2 and CPC negligible.

2.2 Climate models

Simulated historical global climate data are from the Coupled Model Intercomparison Project Phase 6 (CMIP6; Eyring et al. 2016). All CMIP6 global climate models covering the study period (1984-2013) that provided specific humidity and horizontal wind components throughout the troposphere at a daily temporal resolution and surface pressure at a monthly temporal resolution were included in the analysis. While daily

³ CPC Global Unified Precipitation data provided by the NOAA/OAR/ESRL PSL, Boulder, Colorado, USA, from their web site at <https://psl.noaa.gov/data/gridded/data.cpc.globalprecip.html>.

weather variability can change surface pressure at sub-monthly scales making daily surface pressure ideal for computing daily IVT, we use monthly values as a compromise to increase the sample size of CMIP6 models, since most models did not provide daily surface pressure as of the writing of this paper. At the time of writing, eight models met the above criteria. Additionally, daily precipitation is required to compute linked AR precipitation metrics. However, currently one of the eight models used for AR characteristics does not have daily precipitation available (AWI-ESM-1-1-LR). This model is excluded from the precipitation analysis but included in all other analysis. All model data were regridded to a common $1.5^\circ \times 1.5^\circ$ resolution grid via bilinear interpolation.

Chapter 3 Methods

3.1 IVT Calculation

IVT calculations were performed before spatial interpolation at the daily timescale. IVT was calculated from wind and specific humidity fields vertically integrated across all above-ground pressure levels of the following: 300, 500, 700, 850 and 1000 hPa. Since only pressure levels at or above the surface are used, for a given grid cell and day, one or more levels may be unavailable. Given that a significant distance often separates the lowest available pressure level from the surface, IVT values are linearly extrapolated to surface pressure level from the lowest available pressure level. This better accounts for rich moisture and enhanced horizontal winds often present at lower levels within ARs. Comparisons between AR detection results with and without IVT extrapolation showed sensitivity in high elevation regions, where candidate AR objects often failed to meet the $100 \text{ kg m}^{-1} \text{ s}^{-1}$ IVT fixed lower-limit threshold without extrapolation. For some models, it was necessary to interpolate horizontal wind fields prior to IVT calculation such that they were collocated with specific humidity, since there was grid staggering.

3.2 Detection Algorithm

We use the IVT-based tARget version 2 objective AR detection algorithm for AR identification (Guan and Waliser 2018). A summary of key detection criteria follows (for a complete description see Guan and Waliser 2015 and 2018). IVT magnitude must meet a minimum of $100 \text{ kg m}^{-1} \text{ s}^{-1}$ and be above the monthly 85th percentile IVT threshold for that grid cell over the study period, calculated as a 5-month average centered on the

present month. The length of the object must be greater than 2000 km, have a length/width ratio greater than two, and contain a poleward meridional IVT component greater than $50 \text{ kg m}^{-1} \text{ s}^{-1}$. Objects where more than half the grid cells have an IVT direction that deviates by more than 45° from the mean IVT direction are excluded, as well as objects where the mean IVT deviates by more than 45° from the overall object orientation. Additionally, sequentially higher IVT thresholds are applied in 2.5 percentile increments up to the 95th percentile to identify ARs of higher IVT intensity potentially nested within regions of lower IVT that fail to meet the geometry criteria but remain above the 85th percentile.

Dataset-dependent IVT thresholds are used in this study. This allows for AR definition in the context of each model's respective climatology, minimizing the influence of overall IVT biases on AR frequency. In contrast, AR IVT magnitude could show greater sensitivity to overall IVT biases compared to reanalysis-based IVT thresholds—as noted by Guan and Waliser (2017), where the latter was used. The choice here reflects an emphasis on evaluating AR frequency patterns and biases irrespective of general IVT biases, which could inform the interpretation of AR frequency changes in future projections, where a warmer atmosphere will likely increase overall IVT.

The application of the algorithm has impacts on the properties of detected ARs. Since daily timesteps are used in this study, no distinction is made between AR days resulting from multi-day overlap of the same synoptic object versus overlap from a different AR object altogether. Thus, AR frequency does not directly measure the number of unique

AR occurrences, but rather the number of days under which an AR object is spatially coincident with a given grid cell. The model-dependent thresholding means that comparisons between AR objects across models must be interpreted appropriately. Since different IVT thresholds define ARs in each model, the overall IVT biases of each model will have a notable influence on the AR IVT intensity values.

3.3 AR Characteristics and Linked Precipitation

All AR characteristics and precipitation metrics are calculated as 30-year climatologies (1984-2013) at each grid cell over the CONUS. The metrics are the same as those in Slinsky et al. (2020). An extreme precipitation day is defined as any day where the sum of the precipitation for that day and the two preceding days exceeds the 95th percentile of all equivalent non-zero 3-day precipitation totals over the study period. The use of such 3-day totals follows Slinsky et al. (2020) and has the advantage of highlighting prolonged extreme precipitation events—particularly important from an impacts perspective (Ralph and Dettinger 2012)—as well as smoothing any temporal offset between MERRA-2 and CPC reanalyses. A linked extreme precipitation AR day is any AR day that is also an extreme precipitation day. Two AR linked precipitation metrics are used in this study: AR extreme precipitation fraction and AR fraction. They are calculated by normalizing the number of extreme precipitation AR days by the total number of extreme precipitation days or by the total number of AR days, respectively. Examples of both metrics are given in the relevant section below.

Chapter 4 Results

4.1 Atmospheric River Frequency

A day where any part of an AR object is coincident with a grid cell is considered an AR day at that grid cell. For a given season, AR frequency is calculated at each grid cell as the total number of AR days at that grid cell over the study period divided by the number of years in the study period. This yields values in easily interpretable units of (AR) days/season. For example, a DJF AR frequency value of 10 days/season for a particular grid cell means that, on average, the grid cell experienced 10 AR days per winter. Note that multi-day AR objects will be counted once for each day of overlap at a given grid cell, so AR days are not a direct measure of independent AR objects.

Statistical significance for biases is assessed using a two-sided t-test at a 95% confidence level, where the interannual variability provides the variance, as in Payne and Magnusdottir (2015). All statistical significance is calculated this way unless otherwise stated.

Figure 2 shows AR day frequency maps for the multimodel mean. Comparisons between MERRA-2 and CMIP6 (columns (a) and (b), respectively) reveal broad pattern agreement across seasons. Negative and positive statistically significant biases exist (stippling in column (c)), underscoring the influence of both season and location on model performance. Simulations for winter display notable biases over the Southwest and the greater West Coast, where values are exaggerated throughout. The Southwest and

Northern Great Plains multimodel mean NCA region aggregate percent bias values for winter are well above 25 percent (Figure 3), the highest for any region and season.

Negative biases are smaller in magnitude where they occur. These tend to concentrate over the eastern CONUS, with the exception of summer, where they appear in the Northwest and Southwest. Although the Northwest and northern Southwest biases are statistically significant, the region experiences so few ARs in summer that the implications are minimal, especially from an impacts perspective. In winter, the eastern CONUS centered on the Southeast shows negative biases, although these are not statistically significant. The frequency minimum seen in the Northern Great Plains and Midwest is markedly dampened in the multimodel mean, suggesting projected ARs either penetrate beyond the western mountain ranges more often, persist longer when they do, or both.

In spring, the models fail to capture the area of lower AR frequency in the Southwest, while in the Midwest lower frequencies are exaggerated. This simultaneously leads to positive biases over the Southwest and negative biases in the Midwest. Bias distribution for fall is largely the same as winter, although the western CONUS positive biases subside and the negative biases shift from the Southeast to the Northeast.

The NCA region aggregate percent biases for each model (Figure 3) reveal a range of model spread across seasons and regions. The CanESM5 model consistently displays large negative bias, even for regions and seasons when other models are almost all

biased in the opposite direction. The Northern Great Plains region in winter has the largest model spread, with the Southwest and Northern Great Plains overall displaying large spreads for winter and fall. Regions/seasons with the highest model agreement tend to exhibit the smallest error. It is notable that the Southwest in winter—the season when it experiences the most ARs—is also the season with the highest percent bias and model spread, indicating the AR day biases are high both as a percent and in absolute terms. It is noteworthy that the multimodel mean nearly always either outperforms or closely tracks the individual model with the lowest normalized regional bias.

4.2 Atmospheric River Area

AR area is calculated for a grid cell as the median surface area (km^2) of all ARs that had any overlap with that grid cell. The full area of an AR object is used, even if it extends beyond the CONUS. For example, a DJF AR area value for a particular grid cell of $5.5 \times 10^6 \text{ km}^2$ means that the median area of all the winter ARs that passed over that grid cell during the climatological period is $5.5 \times 10^6 \text{ km}^2$. Note again that multi-day AR objects will be counted once for each day of overlap. Thus, for the purposes of this study, the same synoptic AR object is considered a new AR each day.

In this case, since medians are compared, the Mann-Whitney U test is used to assess statistical significance at the 95% confidence level. The rank-based test evaluates whether the distribution of AR area across all days at each grid cell differs significantly between MERRA-2 and the CMIP6 multimodel mean.

Figure 4 shows multimodel mean AR area maps, exhibiting positive biases across all regions and seasons, with summer having the lowest biases. Virtually all biases are statistically significant and nearly all NCA regions/seasons display percent bias values above 20% in the multimodel mean (Figure 5). Winter has the highest biases both as a percent and in absolute terms. Some broad pattern characteristics are captured, such as the maximum in winter covering the Southwest, Northwest, and increasing into the Northern Great Plains. However, pattern agreement is lower than for AR frequency. Note that while there is still considerable model spread in region aggregate percent biases (Figure 5), almost all models show positive biases across seasons and regions. Every instance of negative bias except one comes from the CanESM5 model. This uniform agreement points to systematic overrepresentation of large ARs in the surveyed CMIP6 models. We can confidently state that the models simulate AR area that is on average larger than in MERRA-2 almost uniformly across seasons in the CONUS, especially in winter. Note that winter is the season when ARs already tend to be the largest in MERRA-2. It should also be noted that this does not necessarily directly translate to median AR object size itself displaying commensurate biases, as one AR can be counted multiple times across days. Implications of this are elaborated further in the discussion.

4.3 Atmospheric River Integrated Water Vapor Transport

Figure 6 shows multimodel mean AR IVT maps, revealing strong seasonality and pattern agreement between models and MERRA-2. Compared to AR frequency and area, overall biases are markedly lower in magnitude and opposite in sign (-). The Southwest stands out as an exception, with a winter region aggregate percent bias near 20%—roughly half the percent bias in AR frequency for the same region. Similar to AR frequency, the Northwest exhibits negative biases in the summer, which appear notable when normalized (roughly -20%). However, only about half of the regional grid cells show statistical significance and the low intensity of ARs for the region/season exaggerates the moderate $-40 \text{ kg m}^{-1} \text{ s}^{-1}$ IVT magnitude bias when viewed as a percent. Although individual grid cells might show percent biases extending to -20/+40% for some seasons, high values are generally sporadic and overall NCA region aggregates show good agreement between projections and MERRA-2. Biases in IVT direction are only slightly visually detectable and not statistically significant, although they are most notable over the Colorado Plateau in spring, and California in summer.

Figure 7 reveals that with the exception of winter, models agree overall in showing predominantly negative IVT magnitude biases, although the range of these biases is still considerable. Note that the CanESM5 model is not an outlier for this variable. The multimodel mean NCA percent biases are lowest in IVT magnitude out of all examined variables, near or below +/- ten percent in most cases.

4.4 Linked Atmospheric River Extreme Precipitation

The qualitative distribution of AR extreme precipitation fraction patterns is well captured in the multimodel mean (Figure 8). AR extreme precipitation fraction at a grid cell, reported as a percent, represents the number of extreme precipitation AR days normalized by the total number of extreme precipitation days for a given season. For example, an extreme precipitation fraction value of 70% for a particular grid cell means that 70% of extreme precipitation days are linked to AR days in that location. Overall, there is an overestimation (underestimation) of AR extreme precipitation fraction west (east) of the Rockies. The maxima along the West coast for winter, spring, and fall appear, as do the minima in the Great Plains for all seasons. Statistical significance for biases is sporadic, with two noteworthy exceptions: the Great Basin region in winter and east of the Mississippi in fall (particularly the Southeast). The former is part of a greater pattern of high values (> 80%) found along the West Coast extending beyond the Sierra and Cascades. The minimum over the Northern Great Plains, however, shows close spatial agreement in the models. This suggests ARs in models are perhaps retaining more moisture as they move across the western mountain ranges than in models, widening their ability to produce extreme precipitation over a larger area. We see the higher IVT values in this region/season for projections (Figure 6) that we would expect if this were the case. The lower multimodel mean extreme precipitation linkages coastward of the Sierra/Cascades than in MERRA-2 (Figure 8) are largely due to the influence of one anomalous model (CanESM5), suggesting that the AR extreme

precipitation often linked to orographic uplift in the coastal ranges is still captured and even overestimated in most models (not shown).

AR fraction, shown in Figure 10, represents the number of extreme precipitation AR days normalized by the total number of AR days at a given grid cell. For example, an AR fraction value of 40% for a particular grid cell means that 40% of all AR days are also extreme precipitation days.

The statistically significant negative biases for AR extreme precipitation fraction in the Southeast pairs with statistically significant positive biases in AR fraction (Figure 10), indicating that while simulated AR events are not less likely to produce extreme precipitation, other extreme precipitation mechanisms play a larger role than in observations. This aligns with the negative AR frequency biases (Figure 2) for the same season/region. The reasons behind this shift remain unclear and merit further investigation.

The spatial distribution of the regional biases in AR fraction (Figure 10) trends more positive than those for AR extreme precipitation fraction (Figure 8), meaning ARs are more likely to produce extreme precipitation events in simulations than in MERRA-2. Figures 9 and 11 illustrate the difference as well, where, with the exception of winter, negative biases predominate in the former while positive biases predominate in the latter. Locations where negative AR extreme precipitation fraction biases accompany positive AR fraction biases (e.g. interior Southeast in fall) indicate that more ARs

(relatively) produce extreme precipitation while constituting a smaller portion of overall extreme precipitation.

Much like for AR frequency, in AR extreme precipitation fraction the CanESM5 model deviates drastically from all other models in showing pronounced negative biases for all regions/seasons. Interestingly, this does not hold true for AR fraction, where the same model shows generally positive biases and is in better alignment with other models. This suggests the ARs in CanESM5 are not less likely to produce extreme precipitation than other models, but other mechanisms dominate overall extreme precipitation in contrast to MERRA-2 and other models, possibly due to a scarcity of ARs in the first place.

Chapter 5 Discussion

The primary goal of this study is to identify and quantify biases in AR detection and characterization in CMIP6 climate models. Although an exhaustive diagnosis of the drivers underlying those biases lies beyond the scope of the present evaluation, several germane points merit mention. The notable positive AR frequency biases in the Western CONUS during all seasons except summer do not, on the whole, coincide with commensurate or even same-signed IVT magnitude biases, ruling out a simple IVT bias based explanation for the overestimation of AR frequency. Note that the model-dependent percentile IVT thresholding in the AR detection algorithm already guards against this, but if such a scenario were at play, we would still expect the intensity of ARs to be higher, which we do not uniformly see. This points to potential dynamic processes or thermodynamic influence beyond that reflected in IVT values. Winter in the Southwest NCA region is an exception, where AR IVT and AR frequency biases broadly align. That region notwithstanding, we see large positive frequency biases in regions/seasons where there are minimal or opposing IVT magnitude biases. Both of these suggest discrepancies in IVT do not largely account for AR frequency biases.

A similar conclusion could be reasonably drawn for AR area and AR IVT (Figures 4 and 6). AR IVT correlates even less with the outsized AR area values in projections than with AR frequency, meaning that while models overrepresent larger ARs, they are not typically more intense. Thus, different mechanisms seem to underly AR IVT biases versus AR area/frequency biases. AR area biases show much better alignment with AR frequency

biases than AR IVT biases do. Many of the regions/seasons with high AR frequency biases also display large area biases (e.g. Northern Great Plains in winter), suggesting that the large positive area biases could, in part, account for the positive frequency biases: consistently larger ARs overlap more grid cells on a given day, leading to more AR days even if the number of ARs remains constant. Larger ARs will also take longer to pass over a given grid cell, increasing the likelihood of multi-day overlap. The role of this correspondence, however, should not be overemphasized, as several regions/seasons with significant positive AR area bias do not show commensurate bias in AR frequency—in some cases showing negative bias instead. The same putative dynamic origin of oversized ARs could also influence AR frequency in a parallel but independent fashion, or a separate dynamic cause altogether could be at play.

One other possibility is that ARs are slower moving in models. This could account for higher AR frequency as well as AR area in the models: a slower AR would be more likely to overlap a grid cell for consecutive days, increasing the number of AR days; this would preferentially skew the increase in AR days towards larger ARs, since a slow-moving larger AR will gain more multi-day overlap than an equally slow smaller AR. Differences in the trajectory of AR propagation—distinct from IVT direction—should be considered as well. Regions with negative AR frequency biases and positive AR area biases in the same season (e.g. NW summer and NE winter) indicate that AR area is not driving the frequency bias there. Discrepancies in AR trajectory could account for a reduction in AR

frequency even if AR area is higher. Further research is needed to determine if and to what extent the speed and trajectory of AR propagation plays a role in these biases.

In relation to the wet season in the western CONUS in particular, precipitation processes could influence AR frequency, area, and IVT biases. As suggested above, if simulated ARs retain more moisture when encountering orography, this would bias IVT high and simultaneously allow the AR object to persist for longer, which could increase the number of AR days. The higher IVT values also lend themselves to larger ARs. One possible explanation for this could be loss of orographic lift due to model constraints in resolving complex terrain. This does not necessarily contradict that AR extreme precipitation fraction linkages are still high in this region, as the AR fraction results show that a larger proportion of ARs produce extreme precipitation events. The possibility of inverting cause and effect should also be considered: higher IVT values in ARs could lead to higher AR fraction. However, even with higher baseline IVT, it remains then to explain why AR extreme precipitation fraction is so high in the rain shadow of high mountain ranges.

Chapter 6 Summary and Conclusion

This paper presented an evaluation of AR representation in CMIP6 models for the CONUS, with a focus on NCA subregions. We identified a range of biases in AR characteristics dependent on region, season, and variable examined. The following is a summary of the most salient takeaways:

1. Overall AR frequency patterns are reasonably well represented in the evaluated CMIP6 models, lending confidence to their ability to reproduce broad AR related spatial patterns. Caution should be used when interpreting future changes in AR frequency for the regions of notable biases (see below) due to uncertainty in their causes and possible non-linear scaling under future warming.
2. Notable positive AR frequency biases are present in the Western CONUS for all seasons except summer, with winter biases in the Southwest and Great Plains North particularly high.
3. The Southeast exhibits significant positive frequency biases in spring and summer.
4. The Northeast and Midwest show moderate negative frequency biases in winter and spring, respectively.
5. AR IVT biases tend to be negative and are lowest in magnitude of all examined characteristics, with most regions and seasons below ten percent. The Southwest is an exception, showing positive biases in all seasons except summer.

6. Positive AR Area biases are high across all seasons and regions. In particular, area biases for DJF are exceedingly high, excluding the Southeast and Northeast. Low confidence should be placed in the ability of these CMIP6 models to accurately capture AR area as defined in this study.
7. CMIP6 models reasonably simulate AR extreme precipitation fraction and AR fraction, capturing the principal pattern of both distributions. Significant positive AR extreme precipitation biases are present downwind of the Sierra and Cascades ranges, possibly indicating model constraints in resolving orographic precipitation processes.
8. The CanESM5 model is a major outlier for AR frequency, AR extreme precipitation fraction, and—to a lesser extent—AR area.
9. Taken together, the biases across variables suggests a possible dynamic component to the high AR frequency and AR area biases, although this does not exclude potential concomitant thermodynamic causes. Further research is needed to shed light on these inferred drivers.

It should be noted that reanalysis data is not itself without error. However, its use as an observational dataset is well-established in climate model evaluation studies, as it provides high-quality spatially and temporally continuous historical data (Gelaro et al. 2017). The use of direct observation data instead has precedent in AR studies (e.g. Ralph et al. 2013), but this can only be applied to locations and times with such data, and as a consequence only proves suitable for limited objects of study. Quantifications of

reanalysis data error with reference to AR detection have been performed and can inform model evaluations (e.g. Guan and Waliser 2018). Importantly, Guan and Waliser 2017 found that differences between reanalysis products, on the whole, were substantially smaller than differences between a given reanalysis and projections. Nevertheless, future expansions of this work would benefit from including other reanalysis products and a measure of observational uncertainty.

In the same vein, sensitivities to the choice of AR detection algorithm are well documented (Shields et al. 2018; Rutz et al. 2019; O'Brien et al. 2020). While the applicability of the current study is certainly not confined to work using the Guan and Waliser (2015) algorithm, future research could include a suite of AR detection algorithms alongside multiple reanalysis products to increase the robustness of the results and broaden their relevance.

Table 1. Climate model and reference data used in this study. All climate models are from the Coupled Model Intercomparison Project, Phase 6 (CMIP6). MERRA-2 and CPC are abbreviated for Modern-Era Retrospective Analysis for Research and Applications, Version 2, and Climate Prediction Center, respectively. Horizontal resolution for CMIP6 models is approximate.

CMIP6 Model	Institution (Country)	Horizontal Resolution (latitude x longitude)
AWI-ESM-1-1-LR	Alfred Wegener Institute, Helmholtz Centre for Polar and Marine Research (Germany)	1.875° × 1.875°
BCC-CSM2-MR	Beijing Climate Center (China)	1.125° × 1.125°
CanESM5	Canadian Centre for Climate Modelling and Analysis, Environment and Climate Change Canada (Canada)	2.81° × 2.81°
MIROC6	Japan Agency for Marine-Earth Science and Technology, Atmosphere and Ocean Research Institute, The University of Tokyo, National Institute for Environmental Studies, and RIKEN Center for Computational Science (Japan)	1.41° × 1.41°
MPI-ESM-1-2-HAM	Max Planck Institute for Meteorology (Germany)	1.875° × 1.875°
MPI-ESM1-2-HR	Max Planck Institute for Meteorology (Germany)	0.94° × 0.94°
MPI-ESM1-2-LR	Max Planck Institute for Meteorology (Germany)	1.875° × 1.875°
MRI-ESM2-0	Meteorological Research Institute (Japan)	1.875° × 1.875°
Reference Product		
MERRA-2	National Aeronautics and Space Administration, Global Modeling and Assimilation Office (United States)	0.5° × 0.625°
CPC Daily Precipitation	National Oceanic and Atmospheric Administration Climate Prediction Center (United States)	0.5° × 0.5°



Figure 1. Map of the study region (the CONUS) and the seven NCA sub-regions examined in the research. Figure from Slinsky et al. (2020)

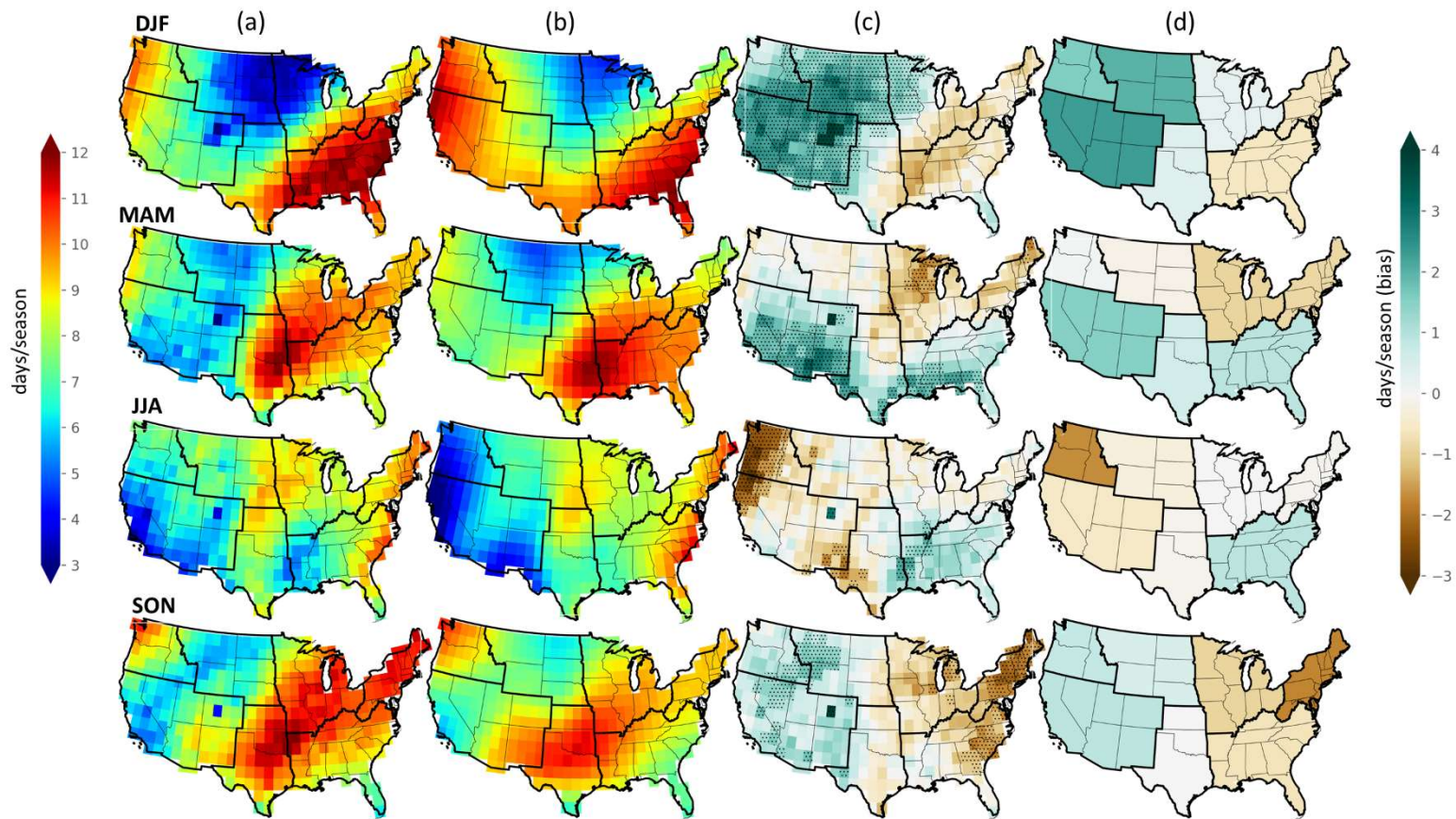


Figure 2. Seasonal AR day frequency maps for the CONUS for (a) MERRA-2, (b) CMIP6, and bias maps for (c) grid points and (d) the NCA regional mean. All values are in units of days/season and each row represents a different meteorological season (winter through fall, from top to bottom). Stippling in column (c) indicates where CMIP6 biases are statistically significant.

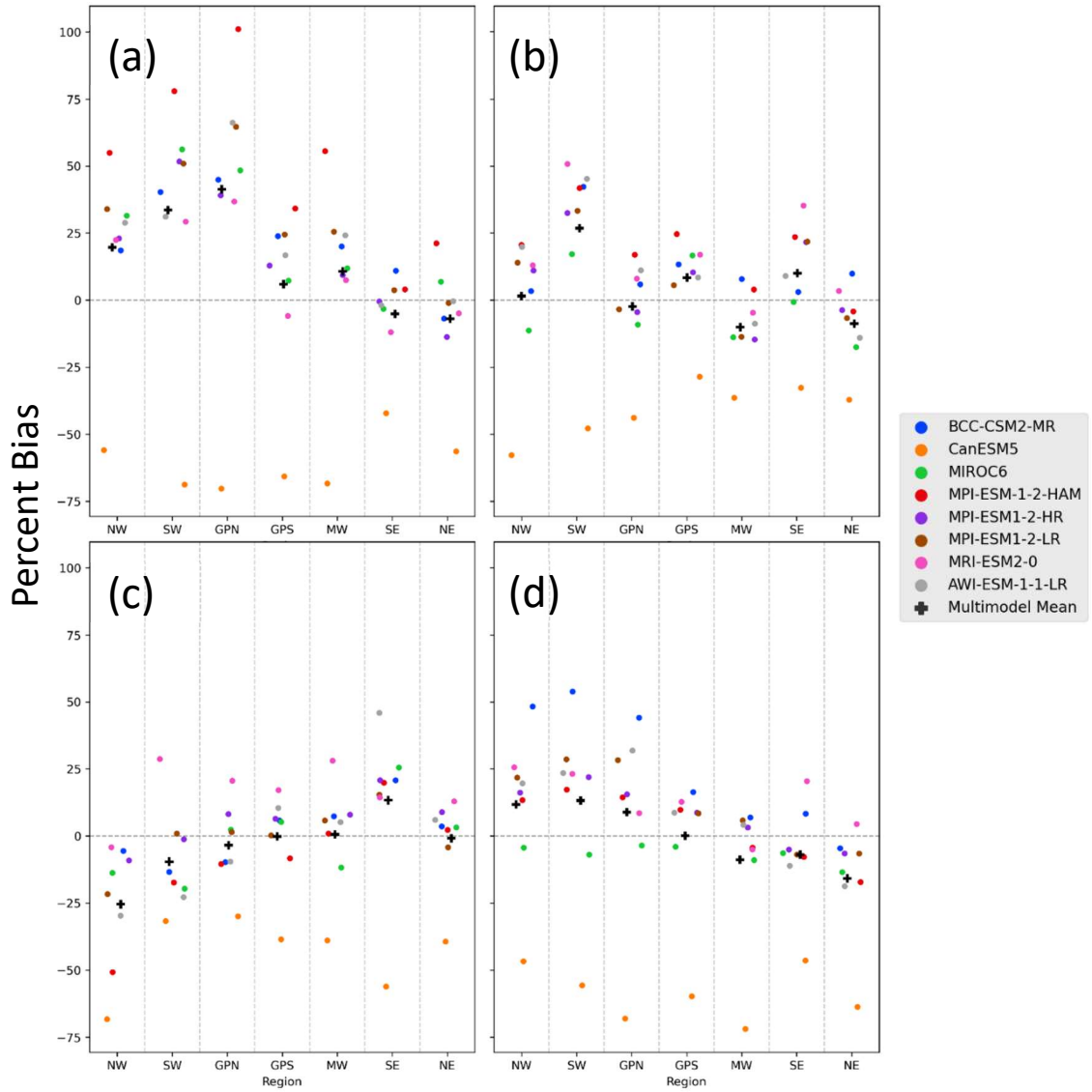


Figure 3. Mean AR frequency percent biases (y-axis) for each NCA region (x-axis) by model for (a) winter, (b) spring, (c) summer, and (d) fall. The multimodel mean is also shown (black cross). Region abbreviations are in Figure 1.

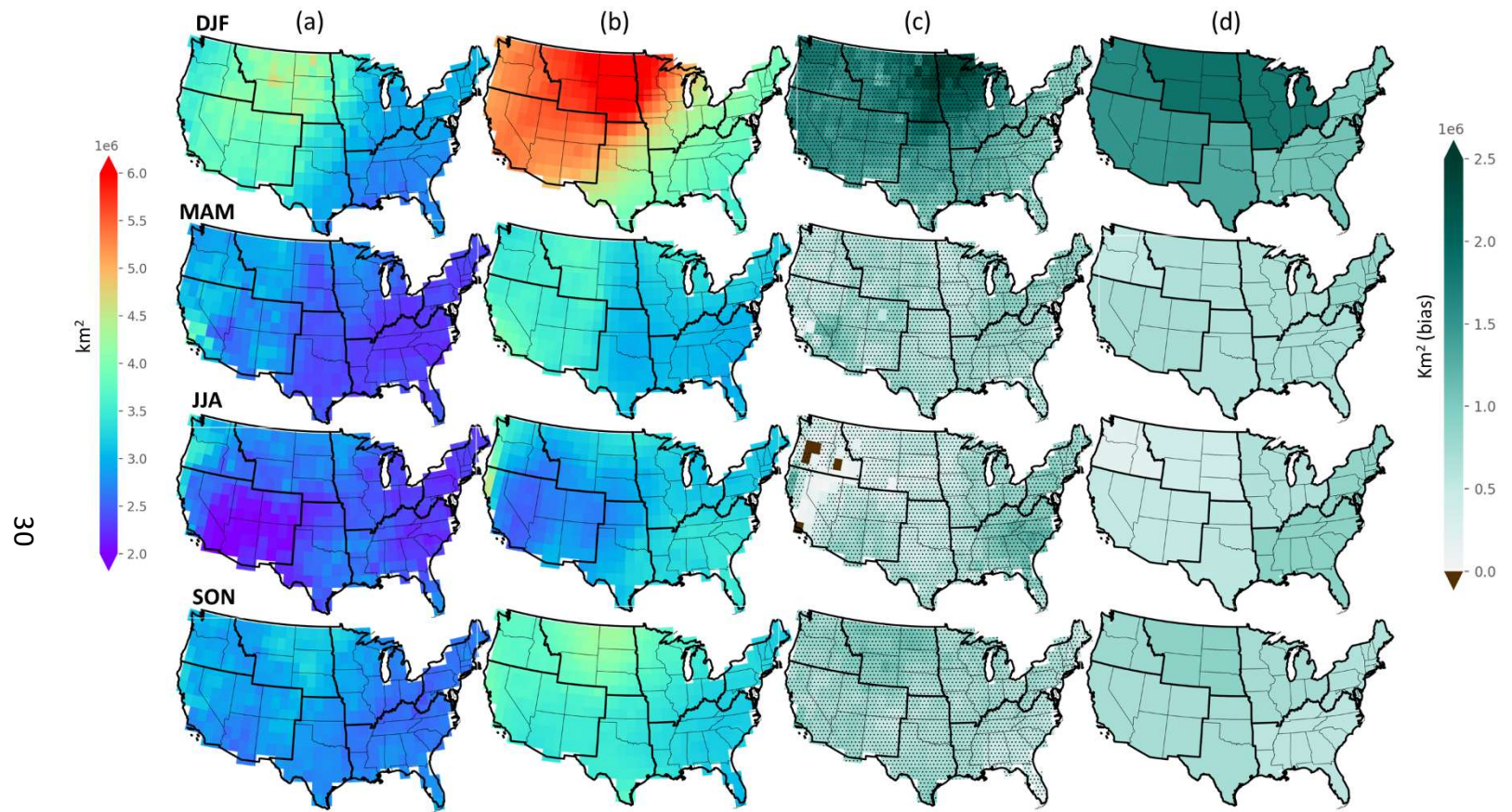


Figure 4. Seasonal median AR area maps for the CONUS for (a) MERRA-2, (b) CMIP6, and bias maps for (c) grid points and (d) the NCA regional mean. All values are in units of km^2 and each row represents a different meteorological season (winter through fall, from top to bottom). Stippling in column (c) indicates where CMIP6 biases are statistically significant.

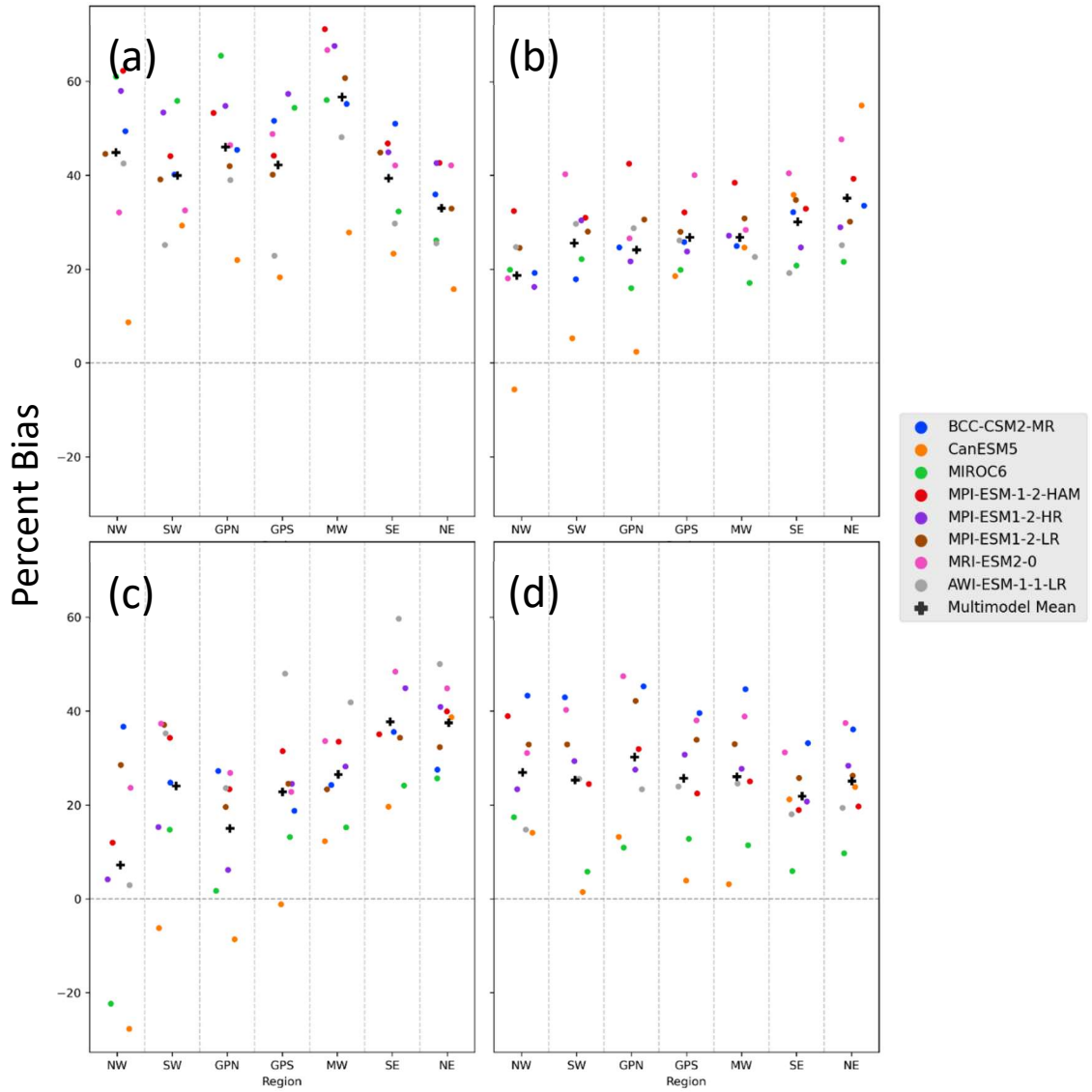


Figure 5. Mean AR area percent biases (y-axis) for each NCA region (x-axis) by model for (a) winter, (b) spring, (c) summer, and (d) fall. The multimodel mean is also shown (black cross). Region abbreviations are in Figure 1.

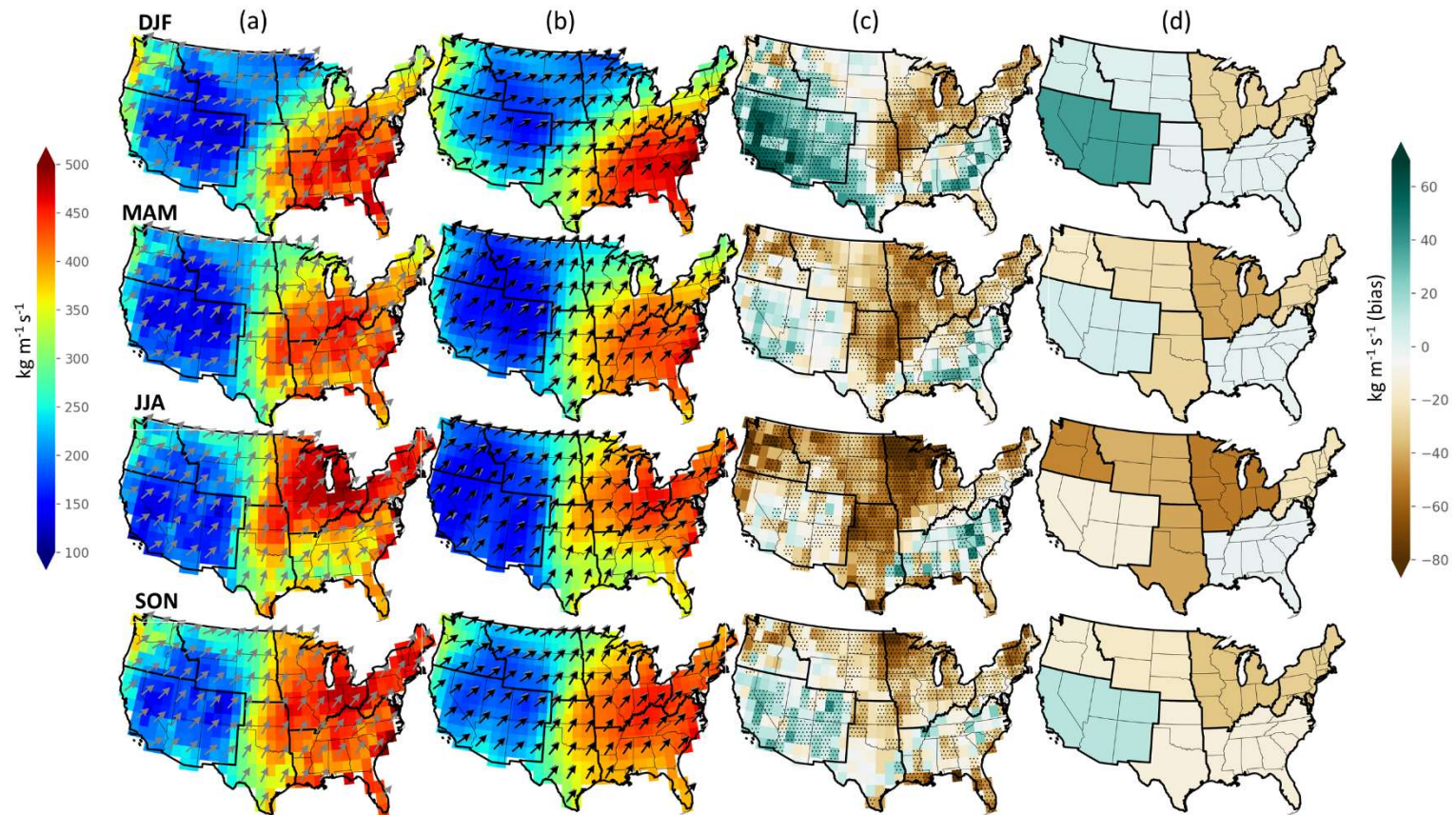


Figure 6. Seasonal AR IVT magnitude (shading) and direction (arrows) maps for the CONUS for (a) MERRA-2, (b) CMIP6, and IVT magnitude bias maps for (c) grid points and (d) the NCA regional mean. In column (b), black arrows show CMIP6 IVT direction while gray arrows underneath show MERRA-2 IVT direction for comparison. All shading values are in units of $\text{kg m}^{-1} \text{s}^{-1}$ and each row represents a different meteorological season (winter through fall, from top to bottom). Stippling in column (c) indicates where CMIP6 IVT magnitude biases are statistically significant.

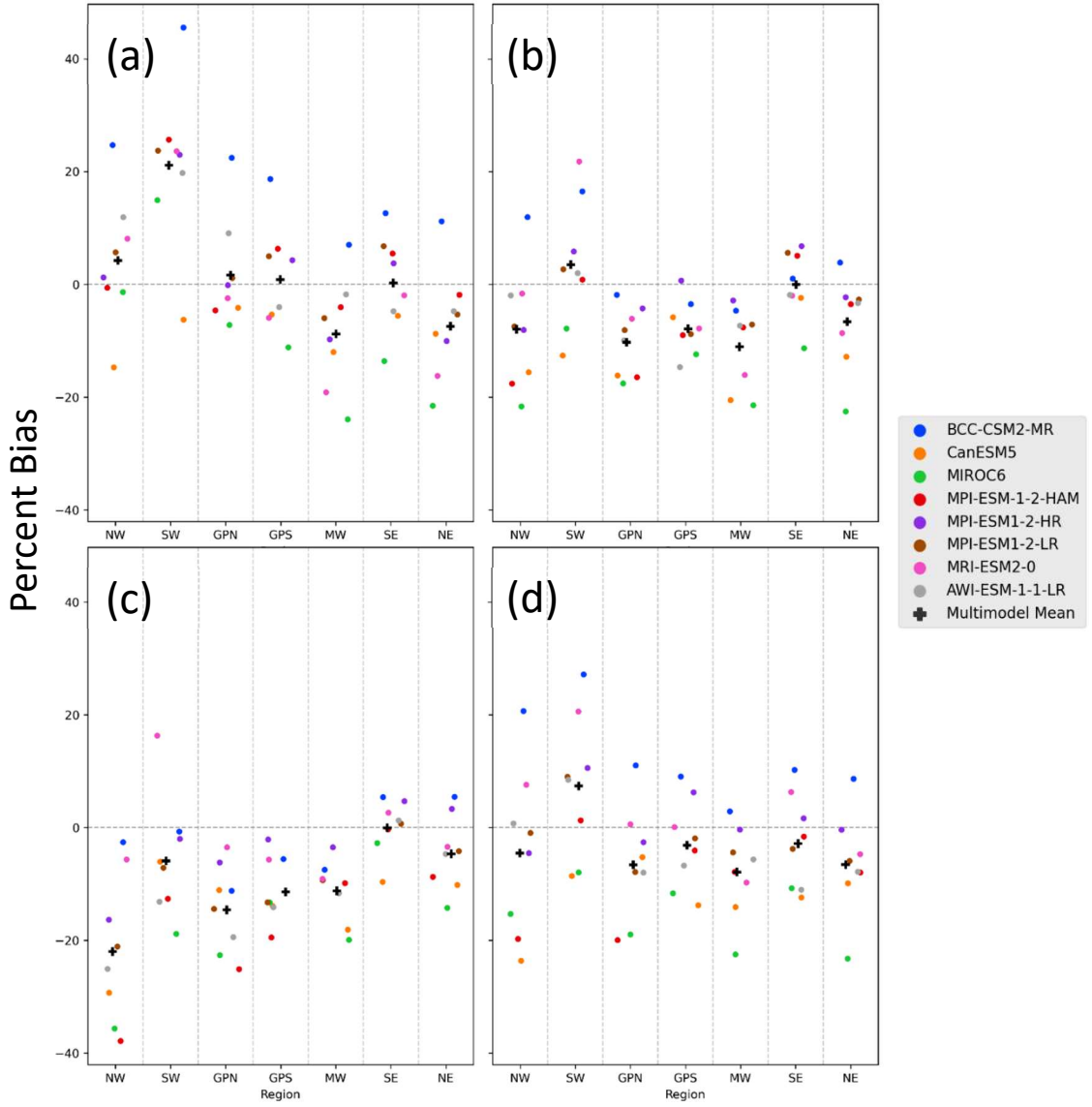


Figure 7. Mean IVT magnitude percent biases (y-axis) for each NCA region (x-axis) by model for (a) winter, (b) spring, (c) summer, and (d) fall. The multimodel mean is also shown (black cross). Region abbreviations are in Figure 1.

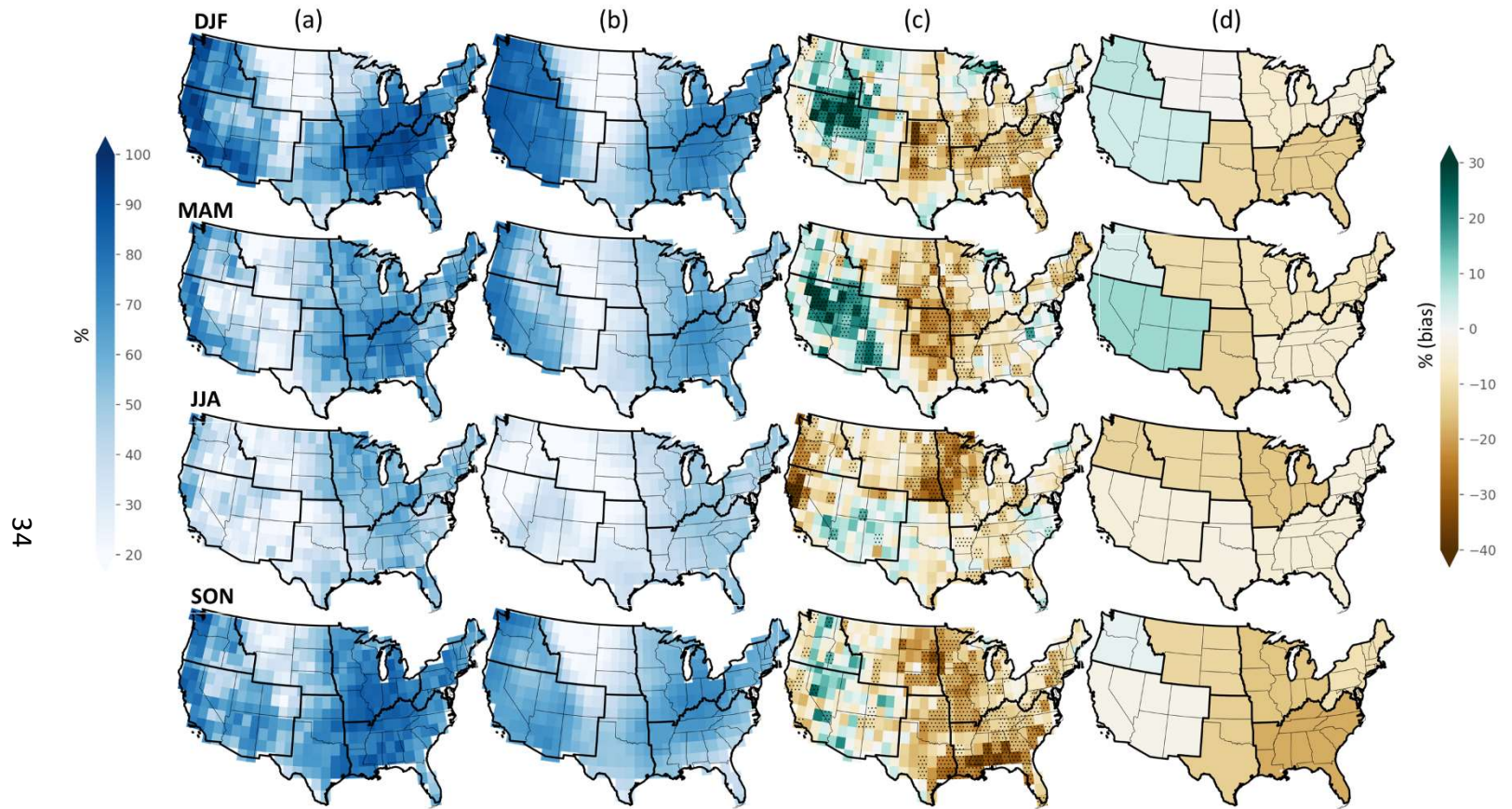


Figure 8. Seasonal AR extreme precipitation fraction maps for the CONUS for (a) MERRA-2, (b) CMIP6, and bias maps for (c) grid points and (d) the NCA regional mean. All values are in units of percent and each row represents a different meteorological season (winter through fall, from top to bottom). Stippling in column (c) indicates where CMIP6 biases are statistically significant.

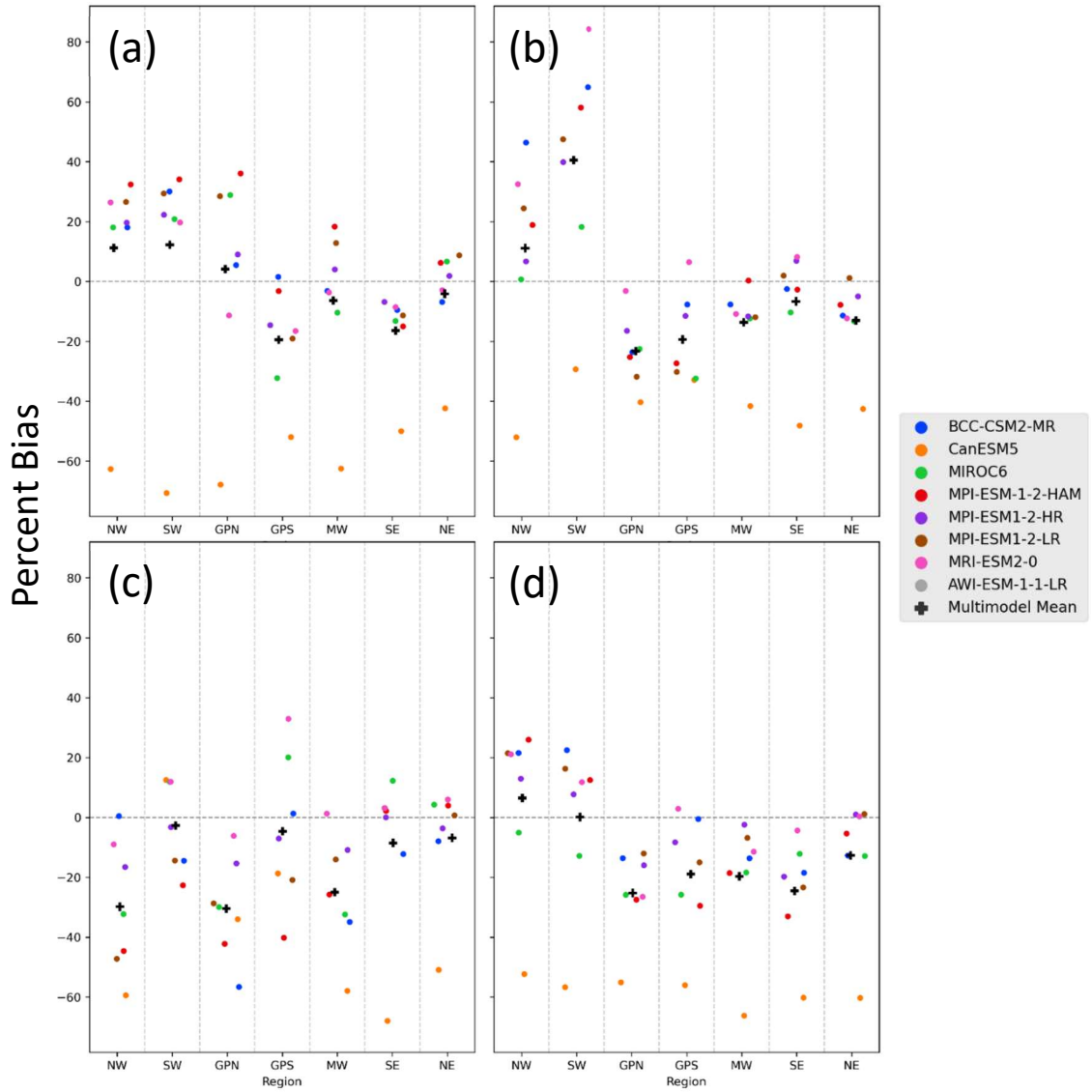


Figure 9. Mean AR extreme precipitation fraction percent biases (y-axis) for each NCA region (x-axis) by model for (a) winter, (b) spring, (c) summer, and (d) fall. The multimodel mean is also shown (black cross). Region abbreviations are in Figure 1.

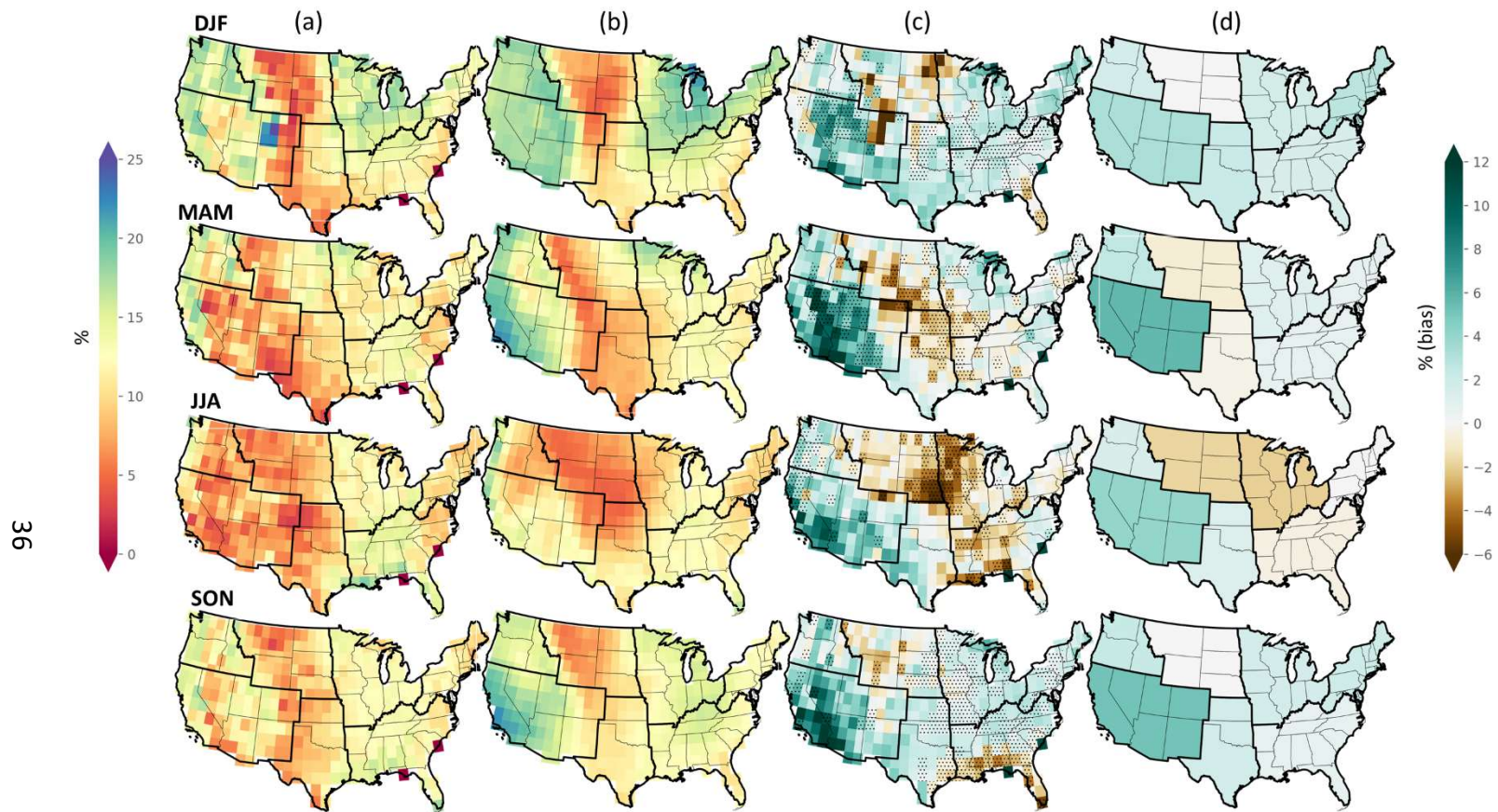


Figure 10. Seasonal AR fraction maps for the CONUS for (a) MERRA-2, (b) CMIP6, and bias maps for (c) grid points and (d) the NCA regional mean. All values are in units of percent and each row represents a different meteorological season (winter through fall, from top to bottom). Stippling in column (c) indicates where CMIP6 biases are statistically significant.

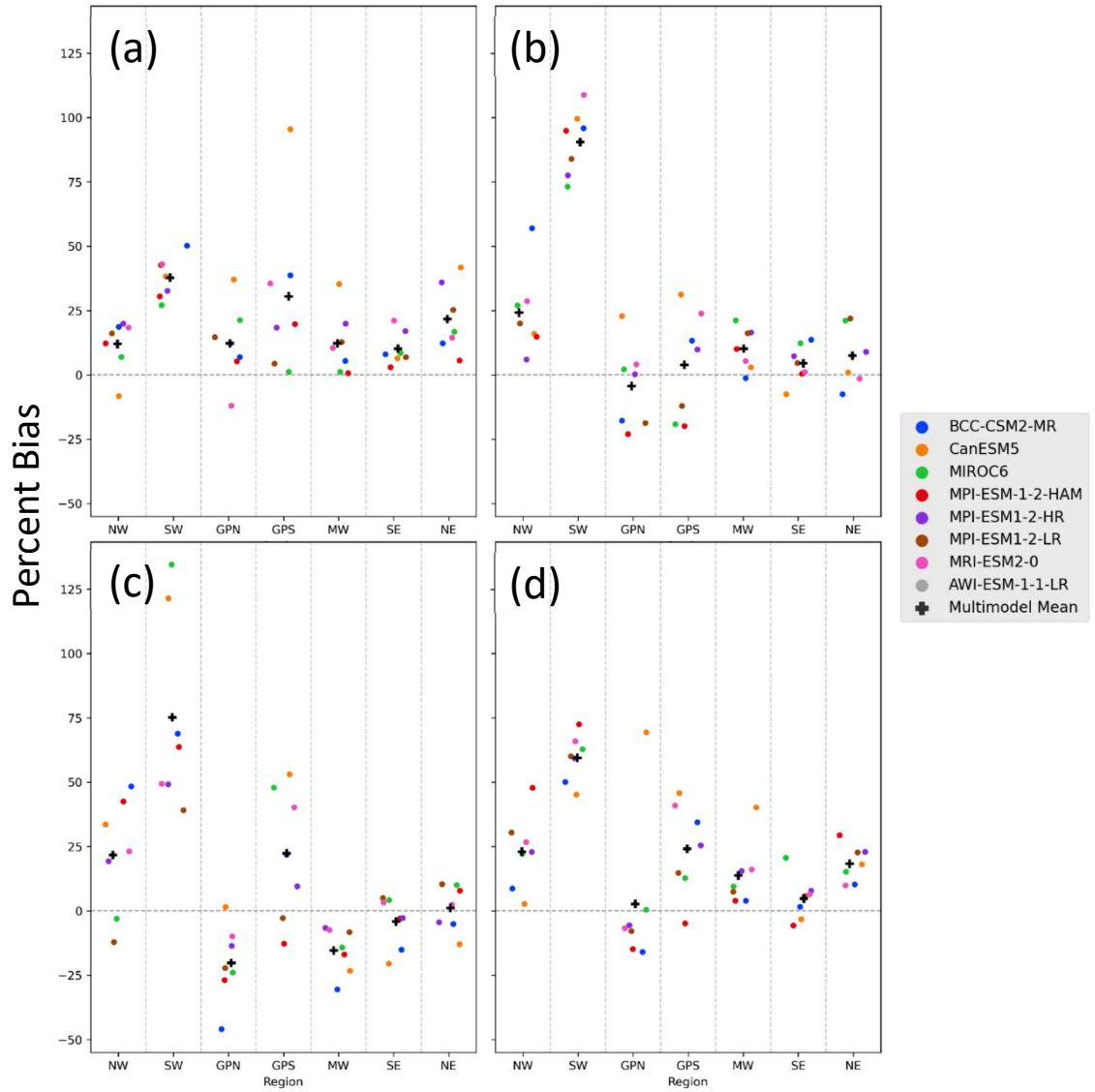


Figure 11. Mean AR fraction percent biases (y-axis) for each NCA region (x-axis) by model for (a) winter, (b) spring, (c) summer, and (d) fall. The multimodel mean is also shown (black cross). Region abbreviations are in Figure 1.

References

- Albano, C. M., M. D. Dettinger, and C. E. Soulard (2017), Influence of atmospheric rivers on vegetation productivity and fire patterns in the southwestern U.S, *Journal of Geophysical Research: Biogeosciences*, 122(2), 308-323.
- Chen, M., P. Xie, and Coauthors (2008), CPC Unified Gauge-based Analysis of Global Daily Precipitation, in *2008 Western Pacific Geophysics Meeting*, edited, Cairns, Australia.
- Chen, M., W. Shi, P. Xie, V. B. S. Silva, V. E. Kousky, R. Wayne Higgins, and J. E. Janowiak (2008), Assessing objective techniques for gauge-based analyses of global daily precipitation, *Journal of Geophysical Research: Atmospheres*, 113(D4).
- Dettinger, M. D. (2013), Atmospheric Rivers as Drought Busters on the U.S. West Coast, *Journal of Hydrometeorology*, 14(6), 1721-1732.
- Dettinger, M. D., F. M. Ralph, T. Das, P. J. Neiman, and D. R. Cayan (2011), Atmospheric Rivers, Floods and the Water Resources of California, *Water*, 3(2), 445-478.
- Dettinger, M. D., et al. (2019), Effects of Atmospheric Rivers, in *Atmospheric Rivers Colloquium Summer School*, edited by F. M. Ralph, M. D. Dettinger, J. J. Rutz and D. Waliser.
- Espinoza, V., D. E. Waliser, B. Guan, D. A. Lavers, and F. M. Ralph (2018), Global Analysis of Climate Change Projection Effects on Atmospheric Rivers, *Geophysical Research Letters*, 45(9), 4299-4308.
- Eyring, V., S. Bony, G. A. Meehl, C. A. Senior, B. Stevens, R. J. Stouffer, and K. E. Taylor (2016), Overview of the Coupled Model Intercomparison Project Phase 6 (CMIP6) experimental design and organization, *Geosci. Model Dev.*, 9(5), 1937-1958.
- Florsheim, J. L., and M. D. Dettinger (2015), Promoting Atmospheric-River and Snowmelt-Fueled Biogeomorphic Processes by Restoring River-Floodplain Connectivity in California's Central Valley, in *Geomorphic Approaches to Integrated Floodplain Management of Lowland Fluvial Systems in North America and Europe*, edited by P. F. Hudson and H. Middelkoop, pp. 119-141, Springer New York, New York, NY.
- Gao, Y., J. Lu, and L. R. Leung (2016), Uncertainties in Projecting Future Changes in Atmospheric Rivers and Their Impacts on Heavy Precipitation over Europe, *Journal of Climate*, 29(18), 6711-6726.
- Gao, Y., J. Lu, L. R. Leung, Q. Yang, S. Hagos, and Y. Qian (2015), Dynamical and thermodynamical modulations on future changes of landfalling atmospheric rivers over western North America, *Geophysical Research Letters*, 42(17), 7179-7186.
- Gelaro, R., et al. (2017), The Modern-Era Retrospective Analysis for Research and Applications, Version 2 (MERRA-2), *Journal of Climate*, 30(14), 5419-5454.
- Guan, B., and D. E. Waliser (2015), Detection of atmospheric rivers: Evaluation and application of an algorithm for global studies, *Journal of Geophysical Research: Atmospheres*, 120(24), 12514-12535.

- Guan, B., and D. E. Waliser (2017), Atmospheric rivers in 20 year weather and climate simulations: A multimodel, global evaluation, *Journal of Geophysical Research: Atmospheres*, 122(11), 5556-5581.
- Guan, B., D. E. Waliser, and F. M. Ralph (2018), An Intercomparison between Reanalysis and Dropsonde Observations of the Total Water Vapor Transport in Individual Atmospheric Rivers, *Journal of Hydrometeorology*, 19(2), 321-337.
- Guan, B., N. P. Molotch, D. E. Waliser, E. J. Fetzer, and P. J. Neiman (2010), Extreme snowfall events linked to atmospheric rivers and surface air temperature via satellite measurements, *Geophysical Research Letters*, 37(20).
- Hagos, S., L. R. Leung, Q. Yang, C. Zhao, and J. Lu (2015), Resolution and Dynamical Core Dependence of Atmospheric River Frequency in Global Model Simulations, *Journal of Climate*, 28(7), 2764-2776.
- Hagos, S. M., L. R. Leung, J.-H. Yoon, J. Lu, and Y. Gao (2016), A projection of changes in landfalling atmospheric river frequency and extreme precipitation over western North America from the Large Ensemble CESM simulations, *Geophysical Research Letters*, 43(3), 1357-1363.
- Hatchett, B. J., S. Burak, J. J. Rutz, N. S. Oakley, E. H. Bair, and M. L. Kaplan (2017), Avalanche Fatalities during Atmospheric River Events in the Western United States, *Journal of Hydrometeorology*, 18(5), 1359-1374.
- Herbst, D. B., and S. D. Cooper (2010), Before and after the deluge: rain-on-snow flooding effects on aquatic invertebrate communities of small streams in the Sierra Nevada, California, *Journal of the North American Benthological Society*, 29(4), 1354-1366.
- Jun, S.-Y., S.-J. Choi, and B.-M. Kim (2018), Dynamical Core in Atmospheric Model Does Matter in the Simulation of Arctic Climate, *Geophysical Research Letters*, 45(6), 2805-2814.
- Khouakhi, A., and G. Villarini (2016), On the relationship between atmospheric rivers and high sea water levels along the U.S. West Coast, *Geophysical Research Letters*, 43(16), 8815-8822.
- Konrad, C. P., and M. D. Dettinger (2017), Flood Runoff in Relation to Water Vapor Transport by Atmospheric Rivers Over the Western United States, 1949–2015, *Geophysical Research Letters*, 44(22), 11,456-411,462.
- Lackmann, G. M. (2013), The South-Central U.S. Flood of May 2010: Present and Future, *Journal of Climate*, 26(13), 4688-4709.
- Lavers, D. A., F. M. Ralph, D. E. Waliser, A. Gershunov, and M. D. Dettinger (2015), Climate change intensification of horizontal water vapor transport in CMIP5, *Geophysical Research Letters*, 42(13), 5617-5625.
- Lavers, D. A., R. P. Allan, G. Villarini, B. Lloyd-Hughes, D. J. Brayshaw, and A. J. Wade (2013), Future changes in atmospheric rivers and their implications for winter flooding in Britain, *Environmental Research Letters*, 8(3), 034010.
- Miller, D. K., D. Hotz, J. Winton, and L. Stewart (2018), Investigation of Atmospheric Rivers Impacting the Pigeon River Basin of the Southern Appalachian Mountains,

- Weather and Forecasting*, 33(1), 283-299.
- Neiman, P. J., L. J. Schick, F. M. Ralph, M. Hughes, and G. A. Wick (2011), Flooding in Western Washington: The Connection to Atmospheric Rivers, *Journal of Hydrometeorology*, 12(6), 1337-1358.
- Newman, M., G. N. Kiladis, K. M. Weickmann, F. M. Ralph, and P. D. Sardeshmukh (2012), Relative Contributions of Synoptic and Low-Frequency Eddies to Time-Mean Atmospheric Moisture Transport, Including the Role of Atmospheric Rivers, *Journal of Climate*, 25(21), 7341-7361.
- Norris, J., A. Hall, D. Chen, C. W. Thackeray, and G. D. Madakumbura (2021), Assessing the Representation of Synoptic Variability Associated With California Extreme Precipitation in CMIP6 Models, *Journal of Geophysical Research: Atmospheres*, 126(6), e2020JD033938.
- Oakley, N. S., J. T. Lancaster, M. L. Kaplan, and F. M. Ralph (2017), Synoptic conditions associated with cool season post-fire debris flows in the Transverse Ranges of southern California, *Natural Hazards*, 88(1), 327-354.
- O'Brien, T. A., et al. (2020), Detection of atmospheric rivers with inline uncertainty quantification: TECA-BARD v1.0.1, *Geosci. Model Dev.*, 13(12), 6131-6148.
- Payne, A. E., and G. Magnusdottir (2015), An evaluation of atmospheric rivers over the North Pacific in CMIP5 and their response to warming under RCP 8.5, *Journal of Geophysical Research: Atmospheres*, 120(21), 11,173-111,190.
- Rabinowitz, L. J., R. A. Lupo, and E. P. Guinan (2018), Evaluating Linkages between Atmospheric Blocking Patterns and Heavy Rainfall Events across the North-Central Mississippi River Valley for Different ENSO Phases, *Advances in Meteorology*, 2018, doi: 10.1155/2018/1217830.
- Radić, V., A. J. Cannon, B. Menounos, and N. Gi (2015), Future changes in autumn atmospheric river events in British Columbia, Canada, as projected by CMIP5 global climate models, *Journal of Geophysical Research: Atmospheres*, 120(18), 9279-9302.
- Ralph, F. M., and M. D. Dettinger (2012), Historical and National Perspectives on Extreme West Coast Precipitation Associated with Atmospheric Rivers during December 2010, *Bulletin of the American Meteorological Society*, 93(6), 783-790.
- Ralph, F. M., T. Coleman, P. J. Neiman, R. J. Zamora, and M. D. Dettinger (2013), Observed Impacts of Duration and Seasonality of Atmospheric-River Landfalls on Soil Moisture and Runoff in Coastal Northern California, *Journal of Hydrometeorology*, 14(2), 443-459.
- Rutz, J. J., et al. (2019), The Atmospheric River Tracking Method Intercomparison Project (ARTMIP): Quantifying Uncertainties in Atmospheric River Climatology, *Journal of Geophysical Research: Atmospheres*, 124(24), 13777-13802.
- Shields, C. A., et al. (2018), Atmospheric River Tracking Method Intercomparison Project (ARTMIP): project goals and experimental design, *Geosci. Model Dev.*, 11(6), 2455-2474.
- Slinskey, E. A., P. C. Loikith, D. E. Waliser, B. Guan, and A. Martin (2020), A Climatology

- of Atmospheric Rivers and Associated Precipitation for the Seven U.S. National Climate Assessment Regions, *Journal of Hydrometeorology*, 21(11), 2439-2456.
- Waliser, D., J. M. Cordeira, M. D. Dettinger, D. A. Lavers, F. Pappenberger, D. S. Richardson, L. J. Schick, and E. Zsoter (2019), AR Modeling: Forecasts, Climate Simulations, and Climate Projections, in *Atmospheric Rivers Colloquium Summer School*, edited by F. M. Ralph, M. D. Dettinger, J. J. Rutz and D. Waliser.
- Warner, M. D., C. F. Mass, and E. P. S. Jr. (2015), Changes in Winter Atmospheric Rivers along the North American West Coast in CMIP5 Climate Models, *Journal of Hydrometeorology*, 16(1), 118-128.
- Xie, P., M. Chen, S. Yang, A. Yatagai, T. Hayasaka, Y. Fukushima, and C. Liu (2007), A Gauge-Based Analysis of Daily Precipitation over East Asia, *Journal of Hydrometeorology*, 8(3), 607-626.
- Young, A. M., K. T. Skelly, and J. M. Cordeira (2017), High-impact hydrologic events and atmospheric rivers in California: An investigation using the NCEI Storm Events Database, *Geophysical Research Letters*, 44(7), 3393-3401.
- Zhao, M. (2020), Simulations of Atmospheric Rivers, Their Variability, and Response to Global Warming Using GFDL's New High-Resolution General Circulation Model, *Journal of Climate*, 33(23), 10287-10303.
- Zhu, Y., and R. E. Newell (1998), A Proposed Algorithm for Moisture Fluxes from Atmospheric Rivers, *Monthly Weather Review*, 126(3), 725-735.